HAL
open science

Crystal chemistry, thermal expansion, and Raman spectra of hydroxyl-clinohumite: implications for water in Earth's interior

Yu Ye, Joseph R. Smyth, Steven D. Jacobsen, Céline Goujon

To cite this version:

Yu Ye, Joseph R. Smyth, Steven D. Jacobsen, Céline Goujon. Crystal chemistry, thermal expansion, and Raman spectra of hydroxyl-clinohumite: implications for water in Earth's interior. Contributions to Mineralogy and Petrology, 2013, 165 (3), pp.563-574. 10.1007/s00410-012-0823-8 . hal-01002000

HAL Id: hal-01002000

https://hal.science/hal-01002000v1

Submitted on 7 Jul 2021

HAL is a multi-disciplinary open access archive for the deposit and dissemination of scientific research documents, whether they are published or not. The documents may come from teaching and research institutions in France or abroad, or from public or private research centers.

L'archive ouverte pluridisciplinaire **HAL**, est destinée au dépôt et à la diffusion de documents scientifiques de niveau recherche, publiés ou non, émanant des établissements d'enseignement et de recherche français ou étrangers, des laboratoires publics ou privés.

Contrib Mineral Petrol (2013) 165:563–574
DOI 10.1007/s00410-012-0823-8

ORIGINAL PAPER

Crystal chemistry, thermal expansion, and Raman spectra of hydroxyl-clinohumite: implications for water in Earth's interior

Yu Ye · Joseph R. Smyth · Steven D. Jacobsen · Céline Goujon

Received: 18 July 2012 / Accepted: 18 October 2012 / Published online: 9 November 2012
© Springer-Verlag Berlin Heidelberg 2012

Abstract Two samples of hydroxyl-clinohumite, sample SZ0407B with approximate composition $Mg_{8.674(14)}Fe_{0.374(4)}(Si_{0.99(1)}O_4)_4(OH)_2$ and sample SZ0411B with composition $Mg_9(SiO_4)_4(OH)_2$, were synthesized at 12 GPa and 1,250 °C coexisting with olivine. Unit-cell parameters determined by single-crystal X-ray diffraction are given as follows: $a = 4.7525(4)$ Å, $b = 10.2935(12)$ Å, $c = 13.7077(10)$ Å, $\alpha = 100.645(9)°$, $V = 659.04(9)$ Å^3 for SZ0407B, and $a = 4.7518(6)$ Å, $b = 10.2861(12)$ Å, $c = 13.7008(9)$ Å, $\alpha = 100.638(9)°$, $V = 658.15(9)$ Å^3 for SZ0411B. Single-crystal X-ray intensity data were collected for crystal structure refinements of both samples. Relative to the pure-Mg sample, Fe decreases M3–OH bond lengths by ~0.010(3) Å, consistent with some ferric iron ordering into M3. Raman spectroscopy shows two strong bands in the lattice-mode region at 650 and 690 cm^{-1} in the Fe-bearing sample, which are not observed in the pure-Mg sample. Spectra in the H_2O region show at least five bands, which are deconvolved into seven distinct O–H-stretching modes. Thermal expansion measurements were carried out for both samples from 153 to 787 K by single-crystal X-ray diffraction. The average *a*-, *b*-, *c*-axial and volumetric thermal expansion coefficients (10^{-6} K^{-1}) are 10.5(1), 12.3(2), 12.5(2) and 34.9(5) for SZ0407B, respectively, and 11.1(1), 12.6(3), 13.7(3), 36.8(6) for SZ0411B, respectively. After heating, the unit-cell parameters were refined again for each sample at ambient condition, and no significant changes were observed, indicating no significant oxidation or dehydration during the experiment. For the DHMS phases along the brucite–forsterite join, linear regression gives a systematic linear decrease in expansivity with increasing density. Further, substitution of ferrous iron into these structures decreases thermal expansivity, making the Fe-bearing varieties slightly stiffer.

Keywords Clinohumite · Crystal structure · Thermal expansion · Iron effect

Communicated by T. L. Grove.

Electronic supplementary material The online version of this article (doi:10.1007/s00410-012-0823-8) contains supplementary material, which is available to authorized users.

Y. Ye (✉)
Department of Physics, University of Colorado, Boulder, CO 80309, USA
e-mail: yuye1@asu.edu

Present Address:
Y. Ye
School of Earth and Space Exploration, Arizona State University, Tempe, AZ 85287, USA

J. R. Smyth
Department of Geological Sciences, University of Colorado, Boulder, CO 80309, USA

S. D. Jacobsen
Department of Earth and Planetary Sciences, Northwestern University, Evanston, IL 60208, USA

C. Goujon
Institut Néel, CNRS et Université Joseph Fourier, BP 166, 38042 Grenoble Cedex 9, France

Introduction

The dense hydrous magnesium silicate (DHMS) minerals along the brucite (Br)–forsterite (Fo) join have been widely studied and proposed as potential carriers of water into the Earth's mantle (McGetchin et al., 1970; Wunder et al., 1995; Kanzaki 1991; Faust and Knittle 1994). These minerals could

also be reservoirs for H_2O in the upper mantle and transition zone in extremely hydrous compositions. These phases include Phase A (2 Fo + 3 Br, 12 wt% H_2O), norbergite (1 Fo + 1 Br, 9 wt% H_2O), chondrodite (2 Fo + 1 Br, 5 wt% H_2O), humite (3 Fo + 1 Br, 4 wt% H_2O), and clinohumite (4 Fo + 1 Br, 3 wt% H_2O). Among these, Phase A ($Mg_7Si_2O_8(OH)_6$), chondrodite ($Mg_7Si_2O_8(OH)_6$), and clinohumite ($Mg_9Si_4O_{16}(OH)_2$) have been observed as dehydration products of serpentine and in experimental studies of pure $MgO–SiO_2–H_2O$ systems at pressures of 5 to 12 GPa (Wunder 1998; Berry and James 2001; Smyth et al. 2006). In the current study, we focus on two synthetic samples of Mg-pure and Fe-bearing (Fe % = 4 mol%) F-free clinohumite by single-crystal X-ray diffraction. In natural high-grade metamorphic rocks and carbonates, clinohumite typically contains F at the hydroxyl site and Ti in one of the octahedral sites. Ferraris et al. (2000) report a natural sample with OH dominant in the OH position. Crystal structure studies have been reported for various clinohumite samples: Ottolini et al. (2000) for natural F-bearing clinohumite, Berry and James (2001) for synthetic Mg-pure clinohumite, and Friedrich et al. (2001) for natural titano-clinohumite by neutron diffraction. Only the monoclinic members of the humite series, clinohumite and chondrodite, have been reported from high-pressure experiments in F-free compositions.

The crystal structure of clinohumite is illustrated in Fig. 1. The space group is $P2_1/b$, which is a nonstandard setting of $P2_1/c$ chosen to preserve the structural similarity to olivine, so that the *a* and *b* axes of olivine and clinohumite are approximately the same. The structure consists of two distinct Si tetrahedral sites, Si1 and Si2, and five distinct octahedral sites, labeled M1c, M1n, M2-5, M2-6, and M3 (Fig. 1). There are nine distinct oxygen positions, each bonded to one Si and three octahedral cations as in olivine, except one monovalent anion site termed OFOH, bonded to three octahedral cations. There are two proton (H) positions possible in F-free clinohumite, one of which is so close to the inversion center that it cannot be fully occupied, so a second position is possible (Berry and James 2001). If present, Ti is strongly ordered into the M3 position to relieve the need for the second proton position and reduce the volume of both the M3 octahedron as well as the unit cell.

In order to evaluate the possible role of clinohumite in subduction environments, it is necessary to have constraints on the equations of state of dense hydrous magnesium silicate phases that might occur in subduction environments as a result of the dehydration of serpentine. Much work has been done on the compressibilities and elasticities of these DHMS phases (Ross and Crichton 2001; Holl et al. 2006; Sanchez-Valle et al. 2006), as well as the thermal expansivities of brucite (Fukui et al. 2003), Phase A (Pawley et al. 1995), and forsterite (Ye et al. 2009). Here, we investigate the effect of iron on the Raman

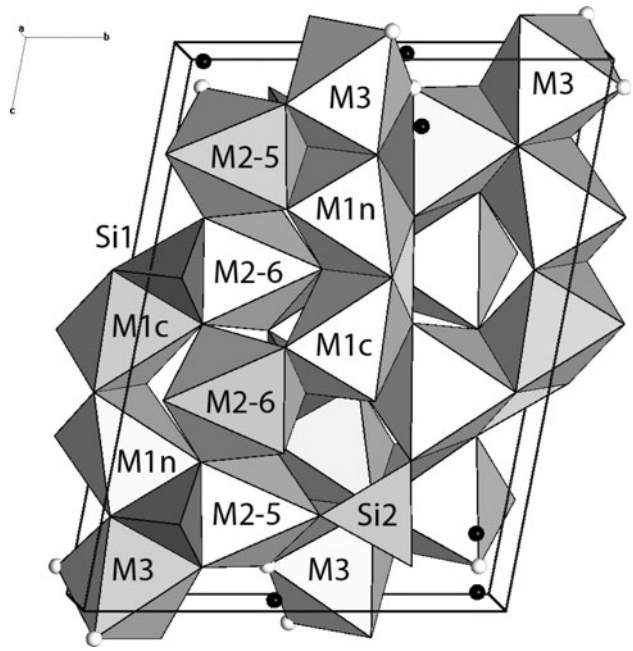

Fig. 1 Crystal structure clinohumite viewed approximately down *a*. The hydroxyl oxygen position is shown as a *white sphere*. The two proton positions are shown as *black spheres*

spectra, thermal expansion, and thermal stability of hydroxyl-clinohumite. Ross and Crichton (2001) showed that the compressibility decreases linearly with increasing density from brucite to forsterite. Here, we show that thermal expansivity also decreases linearly with density along the brucite–forsterite join. We also present crystal structure refinements of two OH-clinohumite samples synthesized at 12 GPa and 1,250 °C: one end-member sample of nominal formula $Mg_9(SiO_4)_4(OH)_2$ and another containing minor amounts of Fe, Mn, Ni, Ti, Ca, and Al.

Experimental procedures

Sample synthesis and composition

The sample SZ0411B is Mg-pure clinohumite, and we assume the stoichiometric composition to be $Mg_9Si_4O_{18}H_2$, whereas the composition of the Fe-bearing sample SZ0407B was analyzed by electron microprobe. Both samples were synthesised at 12GPa and 1,250 °C in double-capsule experiments with two 1.2-mm-diameter welded Pt inner capsules inside a 2-mm outer capsule with the space between capsules packed with brucite to prevent H loss. The two inner capsules had compositions of differing silica activity, one with lower silica giving an assemblage of olivine plus clinohumite and the other giving an assemblage of olivine plus clinoenstatite (Smyth et al. 2006). Starting material for sample SZ0407B was San

Carlos olivine plus silica plus brucite and that for sample SZ0411B was synthetic forsterite, plus silica plus brucite. Sample SZ0407B also contained a small amount of chondrodite which may have resulted from incomplete equilibration between the natural olivine and brucite in the starting material. Oxygen fugacity was not directly buffered during the experiment.

A single crystal about 150 μm from sample SZ0407B was chosen for chemical analysis by electron microprobe. The sample was mounted in epoxy and polished on the surface. Mineral compositions were analyzed using a JEOL 8600 SuperProbe, operating at a 15 kV accelerating voltage and 20 nA beam current, with a 5 μm beam size. Certified mineral standards were used (olivine for Mg, Fe and Si, nickel metal for Ni, garnet for Mn and Al, wollastonite for Ca, ilmenite for Ti). Eighteen points were selected for measuring the weight percentages of oxides, and the average values with standard deviations are listed in Table 1, as well as the weight percentage of H_2O, which was calculated assuming the mole ratio of H:O to be 2:18. The water content is 2.84 wt% for Fe-bearing OH-clinohumite and 2.90 wt% for Mg-pure OH-clinohumite. The formula of sample SZ0407B is summarized as follows: $Mg_{8.674}Fe_{0.374}Ti_{0.001}Mn_{0.005}Ni_{0.011}Al_{0.007}Ca_{0.001}Si_{3.961}O_{18}H_2$, which indicates Fe/(Fe + Mg) = 0.041.

Raman spectroscopy

The same OH-clinohumite crystals used for room-temperature X-ray diffraction experiments were prepared for Raman spectroscopy. Both pure-Mg (run SZ0411B) and Fe-bearing (SZ0407B) OH-clinohumite samples were measured, along with a crystal of OH-chondrodite from SZ0407B for comparison. Crystals were 100–150 μm in size, unpolished, and unoriented. The crystals were cleaned in acetone prior to Raman measurements in order to remove any glue or grease left on the samples from the diffraction mounts. For each composition, unpolarized spectra were obtained from two different, nearly orthogonal directions in the crystals, subsequently called orientation 1 (OR1) and orientation 2 (OR2).

Raman spectra were obtained using a 457-nm diode-pumped, solid-state laser (Melles Griot 85-BLS-601) operating at 250 mW output. Neutral density filters were used to reduce the power to about 2.5 mW at the sample, focused to <5 μm spot size through a 100× objective with a numerical aperture of 0.7. A confocal setup around an Olympus-BX microscope is interfaced with a 0.3 meter Andor Shamrock 303 spectrograph and Newton DU-970 electron multiplying CCD camera (EMCCD). Excitation with a 457-nm source puts bands in the OH-stretching region (3,000–3,600 cm^{-1} shift) at around 530–550 nm, which is where our EMCCD has the highest quantum efficiency. Spectra were collected either using 1,200 lines/mm or 1,800 lines/mm diffraction gratings. All the spectra were collected using a 60-s acquisition time, averaged over five accumulations.

Table 1 Results of electron microprobe analyses for SZ0407B, compared with calculated results for SZ0411B ($Mg_9Si_4O_{18}H_2$)

	SZ0407B	SZ0411B[a]		SZ0407B	SZ0411B[a]
SiO_2 (wt%)	37.53(9)	38.70	Si (apfu)	3.961(9)	4
TiO_2	0.014(4)	–	Ti	0.0011(3)	–
Al_2O_3	0.053(2)	–	Al	0.0066(2)	–
MgO	55.12(9)	58.40	Mg	8.674(14)	9
FeO	4.24(5)	–	Fe	0.374(4)	–
NiO	0.131(6)	–	Ni	0.011(1)	–
MnO	0.057(2)	–	Mn	0.0051(2)	–
CaO	0.008(2)	–	Ca	0.0008(2)	–
H_2O[b]	2.84	2.90	H[b]	2	2
Total	100.00(3)	100			

[a] Data for SZ0411B are calculated from stoichiometry

[b] The wt% and apfu values for H_2O/H are calculated from stoichiometry, assuming the mole ratio of H:O to be 2:18

Crystal structure

Two single crystals from the samples of SZ0407B and SZ0411B were selected for X-ray intensity measurements at ambient conditions, and crystal sizes were about 110 × 100 × 90 μm^3 for SZ0407B; 110 × 95 × 80 μm^3 for SZ0411B. First, the unit-cell parameters of each crystal were refined using a Bruker P4 four-circle diffractometer with a dual scintillation point detector system, which used an 18 kW rotating Mo-anode X-ray generator operated at 50 kV and 250 mA. Mo$K\alpha_1 - K\alpha_2$ mixed characteristic wavelength was used with $K\alpha$_avg = 0.71080 Å, which was calibrated by a single crystal of anhydrous forsterite of spherical shape. In total, diffractometer angles for 40 reflections were refined, with unique indices $(0\bar{2}1)$, $(0\bar{2}2)$, $(0\bar{2}3)$, $(14\bar{1})$, $(22\bar{5})$, $(13\bar{1})$, (114), (124), $(02\bar{3})$, $(1\bar{3}3)$, $(1\bar{4}1)$, $(1\bar{3}1)$, (022), (004), (009), $(0\bar{6}6)$, (324) and (224).

Intensity data for both single crystals were collected using a Bruker APEX II CCD detector mounted on a P4 diffractometer, with the 2θ scan ranges <60°. Refinements of atom positions and anisotropic displacement parameters were done using the program SHELXL-97 (Sheldrick 1997) in the software package WinGX (Farrugia 1999). We used scattering factors of Mg^{2+}, Fe^{2+} and Si^{4+} reported by Cromer and Mann (1968), and those of O^{2-} from Tokonami (1965). Friedrich et al. (2001) reported only one proton position in the crystal structures of natural F-bearing clinohumite samples by single-crystal neutron diffraction, whereas Berry and James (2001) observe two deuterium positions (D1 and D2) in the internal structure of synthetic

Table 2 Unit-cell parameters and intensity data collection parameters at ambient condition

	SZ0407B	SZ0411B		SZ0407B	SZ0411B
a (Å)	4.7525(4)	4.7518(6)	No. total reflections	9,222	8,962
b (Å)	10.2935(12)	10.2861(12)	No. unique total	1,933	1,963
c (Å)	13.7077(10)	13.7008(9)	No. unique $I > 4\sigma$	1,604	1,323
α (°)	100.645(9)	100.638(9)	GooF	0.744	0.877
V (Å^3)	659.04(9)	658.15(9)	R_1 for all (%)	3.26	6.87
			R_1 for $I > 4\sigma$ (%)	2.42	3.83
			R_{int} (%)	2.49	4.95

deuterated F-free clinohumite sample by powder neutron diffraction. For both the current samples SZ0407B and SZ0411B, we attempted to refine H1 and H2 positions, assuming full occupancies in proton positions, and isotropic vibration of protons with U_{eq} fixed at 0.05. However, the contribution of H cations to the X-ray reflection intensities is very small, causing little effect on the refinements of the positions for other heavier atoms. The intensity data collection parameters for both samples are listed in Table 2, as well as the unit-cell parameters at ambient condition, and the refined atomic position coordinates and occupancy factors are shown in Table 3, and the anisotropic displacement parameters are listed in Table 4. In Table 3, the refined occupancies of Mg, Fe cations for the sample SZ0407B are shown, assuming the total occupancy of Mg + Fe to be 1 at each octahedral site. Since the electron microprobe results give an average occupancy of 99 % for Si in SZ0407B structure, the Si occupancies in the tetrahedral sites are refined for both the samples. In addition, the occupancies of all O^{2-} anions are fixed at 1. The cif files for structure refinements of both samples are deposited in the supplementary materials: MOESM1 and MOESM2.

Thermal expansion

After structure refinement at ambient conditions, both single crystals were used for thermal expansion studies at low and high temperatures at ambient pressure. At each temperature step, the unit-cell parameters were refined using the same procedure at ambient temperature described above. Three low-temperature measurements were conducted at 253, 203, and 153 K. Low temperatures were measured and controlled by an LT-2A controller, which uses a low-temperature N_2 gas stream. Next, the single crystals were transferred inside silica glass capillary for high-temperature experiments. Ten high-temperature steps were taken for measurements, up to 787 K, using a Bruker high-temperature device, which uses a two-prong ceramic-coated Pt wire radiant heater, with an Omega temperature-control unit. Ye et al. (2009) reported the temperature calibrations in details. The unit-cell parameters at temperatures are listed in Appendix 1.

Table 3 Atomic position coordinates and occupancy factors

	x	*y*	*z*	Refined occupancy	
				Mg	Fe
SZ0407B					
M1C	0.5	0	0.5	0.973(4)	0.027(4)
M1N	0.4952(1)	0.94692(5)	0.27538(4)	0.963(3)	0.037(3)
M25	0.0079(1)	0.14254(5)	0.17177(4)	0.968(3)	0.032(3)
M26	0.5087(1)	0.25066(5)	0.38852(4)	0.972(3)	0.028(3)
M3	0.4882(1)	0.87609(5)	0.04227(4)	0.955(3)	0.045(3)
Si1	0.0730(1)	0.06692(4)	0.39015(3)	0.978(4)	
Si2	0.0782(1)	0.17314(4)	0.83357(3)	0.990(4)	
O11	0.7329(2)	0.0649(1)	0.38859(8)		
O12	0.2794(2)	0.4205(1)	0.38853(9)		
O13	0.2228(2)	0.1136(1)	0.29428(9)		
O14	0.2221(2)	0.1588(1)	0.48669(9)		
O21	0.2387(2)	0.3250(1)	0.16481(8)		
O22	0.7753(2)	0.9713(1)	0.16454(9)		
O23	0.7254(2)	0.2818(1)	0.26350(9)		
O24	0.7283(2)	0.2298(1)	0.07223(9)		
OFOH	0.2635(3)	0.0487(1)	0.0584(1)		
H1	0.098(13)	0.004(7)	0.023(5)		
H2	0.452(14)	0.101(6)	0.130(5)		
SZ0411B					
M1C	0.5	0	0.5		
M1N	0.4949(2)	0.9471(1)	0.27533(7)		
M25	0.0071(2)	0.1430(1)	0.17218(7)		
M26	0.5083(2)	0.2507(1)	0.38875(7)		
M3	0.4875(2)	0.8751(1)	0.04259(7)		
Si1	0.0727(2)	0.06683(8)	0.39015(6)	0.987(5)	
Si2	0.0786(2)	0.17287(8)	0.83331(6)	0.993(5)	
O11	0.7331(4)	0.0655(2)	0.3885(1)		
O12	0.2794(4)	0.4208(2)	0.3886(1)		
O13	0.2234(4)	0.1133(2)	0.2945(1)		
O14	0.2229(4)	0.1584(2)	0.4865(1)		
O21	0.2391(4)	0.3252(2)	0.1648(1)		
O22	0.7748(4)	0.9715(2)	0.1646(1)		
O23	0.7248(4)	0.2823(2)	0.2637(1)		
O24	0.7278(4)	0.2295(2)	0.0726(1)		
OFOH	0.2643(5)	0.0495(2)	0.0589(2)		
H1	0.13(2)	0.007(10)	0.030(7)		
H2	0.48 (2)	0.109(9)	0.147(7)		

Table 4 Anisotropic displacement parameters (Å^2)

	U_{11}	U_{22}	U_{33}	U_{23}	U_{13}	U_{12}	U_{eq}
SZ0407B							
M1C	0.0058(4)	0.0086(4)	0.0060(4)	0.0020 (3)	−0.0008(3)	−0.0004(3)	0.0067(3)
M1N	0.0060(3)	0.0082(3)	0.0066(3)	0.0002(2)	0.0007(2)	0.0003(2)	0.0071(2)
M25	0.0087(3)	0.0070(3)	0.0079(3)	0.0016(2)	−0.0008(2)	0.0001(2)	0.0078(2)
M26	0.0073(3)	0.0058(3)	0.0074(3)	0.0012(2)	−0.0004(2)	−0.0004(2)	0.0068(2)
M3	0.0076(3)	0.0100(3)	0.0077(3)	0.0022(2)	−0.0004(2)	0.0007(2)	0.0084(2)
Si1	0.0039(2)	0.0054(2)	0.0055(3)	0.0009(2)	−0.0002(1)	−0.0001(1)	0.0050(2)
Si2	0.0043(2)	0.0052(2)	0.0057(3)	0.0009(2)	−0.0001(1)	0.0000(1)	0.0051(2)
O11	0.0053(6)	0.0073(5)	0.0067(6)	0.0012(4)	0.0010(4)	0.0001(4)	0.0064(3)
O12	0.0064(5)	0.0069(5)	0.0069(6)	0.0010(4)	0.0000(4)	0.0012(4)	0.0068(3)
O13	0.0064(6)	0.0074(5)	0.0062(6)	0.0022(4)	0.0004(4)	0.0004(4)	0.0065(3)
O14	0.0066(6)	0.0063(5)	0.0078(6)	0.0006(4)	0.0001(4)	0.0000(4)	0.0070(3)
O21	0.0055(6)	0.0077(5)	0.0064(6)	0.0009(4)	0.0000(4)	0.0003(4)	0.0066(3)
O22	0.0074(6)	0.0066(5)	0.0075(6)	0.0013(4)	0.0006(4)	0.0002(4)	0.0072(3)
O23	0.0060(5)	0.0077(5)	0.0071(6)	0.0022(4)	0.0003(4)	0.0001(4)	0.0068(3)
O24	0.0071(6)	0.0061(5)	0.0067(6)	0.0000(4)	0.0001(4)	−0.0002(4)	0.0068(3)
OFOH	0.0170(7)	0.0084(6)	0.0199(7)	0.0044(5)	0.0111(6)	0.0036(5)	0.0149(3)
SZ0411B							
M1C	0.0059(7)	0.0103(7)	0.0062(6)	0.0019(5)	−0.0009(5)	0.0003(6)	0.0074(3)
M1N	0.0069(5)	0.0081(5)	0.0077(4)	−0.0007(4)	0.0005(4)	0.0004(4)	0.0078(2)
M25	0.0088(5)	0.0067(5)	0.0085(5)	0.0008(4)	−0.0006(4)	−0.0002(4)	0.0080(3)
M26	0.0066(5)	0.0058(5)	0.0086(5)	0.0008(4)	0.0002(4)	−0.0006(4)	0.0071(2)
M3	0.0079(5)	0.0093(5)	0.0096(5)	0.0022(4)	−0.0006(4)	0.0010(4)	0.0089(2)
Si1	0.0053(4)	0.0058(4)	0.0065(4)	0.0007(3)	−0.0001(3)	−0.0004(3)	0.0059(2)
Si2	0.0059(4)	0.0056(4)	0.0067(4)	0.0005(3)	0.0003(3)	0.0000(3)	0.0062(3)
O11	0.005(1)	0.007(1)	0.0076(9)	0.0010(8)	0.0006(7)	−0.0007(8)	0.0064(4)
O12	0.008(1)	0.006(1)	0.0084(9)	−0.0004(8)	−0.0009(8)	0.0009(8)	0.0079(4)
O13	0.005(1)	0.006(1)	0.0091(9)	0.0009(8)	−0.0015(8)	−0.0004(8)	0.0070(4)
O14	0.006(1)	0.008(1)	0.0079(9)	−0.0009(8)	0.0003(8)	−0.0004(8)	0.0077(3)
O21	0.006(1)	0.005(1)	0.0074(9)	0.0020((8)	−0.0002(7)	−0.0002(8)	0.0062(4)
O22	0.007(1)	0.007(1)	0.0098(9)	0.0011(8)	0.0006(8)	−0.0008(8)	0.0079(4)
O23	0.006(1)	0.008(1)	0.0087(9)	0.0020(8)	0.0003(8)	−0.0015(8)	0.0076(4)
O24	0.007(1)	0.008(1)	0.0080(9)	0.0014(8)	−0.0001(8)	−0.0007(8)	0.0077(4)
OFOH	0.020(1)	0.008(1)	0.021(1)	0.0037(9)	0.011(1)	0.0014(9)	0.0160(5)

Results and discussion

Raman spectroscopy

Unpolarized Raman spectra of OH-clinohumites SZ0407B and SZ041B are shown in Fig. 2, along with a spectrum of coexisting OH-chondrodite from run SZ0407B for comparison. Because the Raman spectra of OH-clinohumite and OH-chondrodite are very similar, and nearly identical in the OH-stretching region (Fig. 2), the most distinguishing difference occurs between 800 and 900 cm^{-1}, where OH-clinohumite has three strong bands and OH-chondrodite only displays one strong band. In Fig. 3, we identify the major difference between pure-Mg and Fe-bearing OH-clinohumite as the presence of a strong band pair at 650 and 690 cm^{-1} in the Fe-bearing sample, and therefore likely associated with Fe–O lattice vibrational modes. In Fig. 4, we compare the spectra of pure-Mg and Fe-bearing OH-clinohumites in the 780–1,000 cm^{-1} range. For each composition, unpolarized spectra are shown for two different, roughly orthogonal directions, that is, the laser is focused on surfaces roughly 90-degrees apart, called orientation 1 (OR1) and orientation 2 (OR2) to illustrate some variability with direction. Aside from differences in band intensities with orientation, the spectra are similar with vibrational band positions identical within error between pure-Mg and Fe-bearing OH-clinohumite. Fig. 5a illustrates Raman spectra for the OH-clinohumite

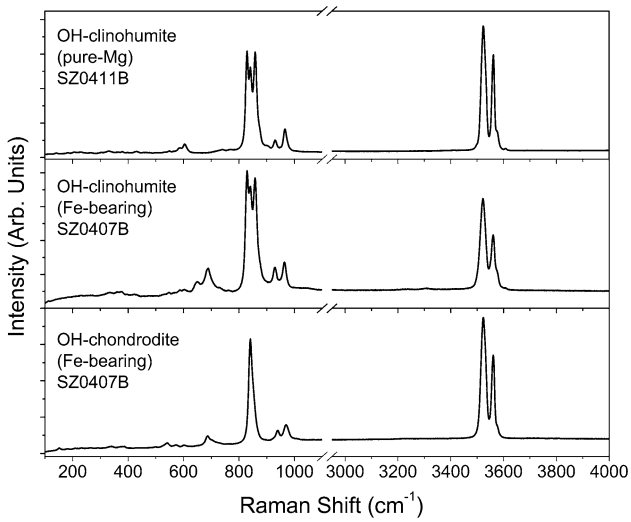

Fig. 2 Comparison of unpolarized Raman spectra for pure-Mg OH-clinohumite (*top panel*), Fe-bearing OH-clinohumite (*middle panel*), and OH-chondrodite (*bottom panel*) coexisting with OH-clinohumite from run SZ0407B

samples in the OH-stretching region. Peaks in the OH-stretching region for the Mg-pure sample agree with those reported by Lin et al. (2000), who observed two strong bands at 3,527 and 3,564 cm^{-1}.The two primary OH peaks in our spectra occur at about 3,522 and 3,560 cm^{-1}. Also in agreement with Lin et al. (2000), the spectra show a shoulder on the 3,560 band at about 3,575 cm^{-1}, and there is a minor band at 3,608 cm^{-1}, also reported by Lin et al. (2000) at 3,610 cm^{-1}. The position of these bands is also consistent with OH-stretching spectra measured by FTIR spectroscopy (Liu et al. 2003). In addition to these four main OH bands, we observe a weak band at about 3,500 cm^{-1}, most easily seen in OR1 of the Fe-bearing sample SZ0407B (Fig. 5a).

In Fig. 5b, c, we show deconvolution of the Raman spectra in the OH-stretching region for samples SZ0411B and SZ0407B, respectively. The need for a second peak in the 3,522 cm^{-1} band is best seen in Fig. 5a for the pure-Mg sample, where an asymmetry is observed on the high-wavenumber side of the 3,522 cm^{-1} peak. For this main band, we fitted a pair of peaks at 3,523 and 3,533 cm^{-1} for the pure-Mg sample (Fig. 5b) and a band pair at 3,520 and 3,532 cm^{-1} in the Fe-bearing sample (Fig. 5c). Although the resolution of these spectra is about 1 cm^{-1}, the small shift of a few wavenumbers for the 3,522 cm^{-1} OH band for the Fe-bearing sample is clearly seen in the stacking of the spectra in Fig. 5a. In total, we resolve seven OH-stretching bands for Mg and Fe-bearing OH-clinohumites, located at about 3,500, 3,522, 3,533, 3,555, 3,562, 3,575, and 3,608 cm^{-1}.

Crystal structure

Based on the refined occupancies of cations in sample SZ0407B in Table 3, Fe/(Fe + Mg) = 4.5 mol% in M3 site, compared to about 3 % in the other M sites. On average, Fe/(Fe + Mg) = 3.6 % from X-ray intensity scan, which is slightly smaller than 4.1 % obtained from electron microprobe analyses in the previous discussion (Table 1). Robinson et al. (1973) reported lower Fe contents in the M3 site for F-bearing clinohumite (Fe % = 5.6 % and F % = 5.8 %) and higher Fe content in

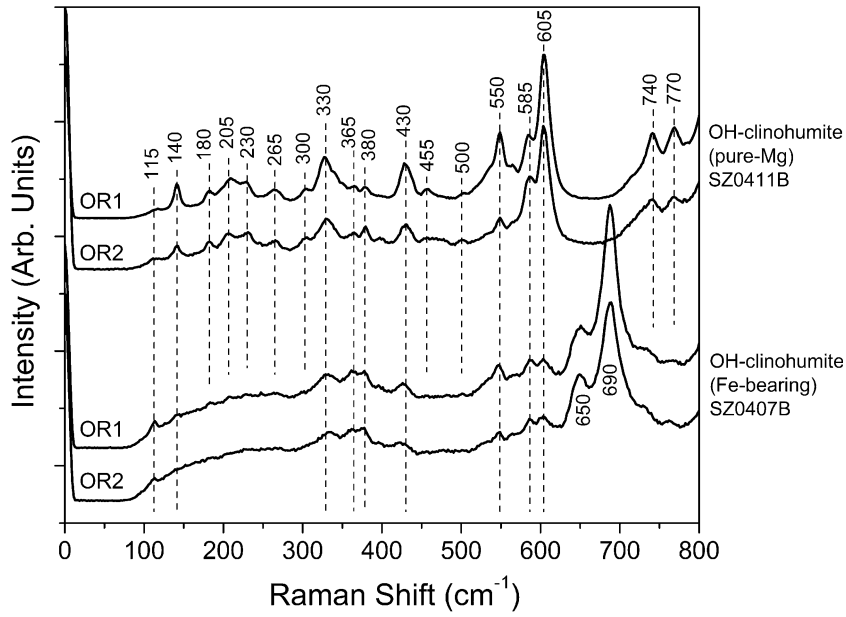

Fig. 3 Comparison of unpolarized Raman spectra between Mg-pure and Fe-bearing OH-clinohumite. The laser was focused on two roughly perpendicular surfaces for orientation 1 (OR1) and orientation 2 (OR2). The major difference in the Fe-bearing OH-clinohumite sample is the appearance of the band pair at 650 and 690 cm^{-1}

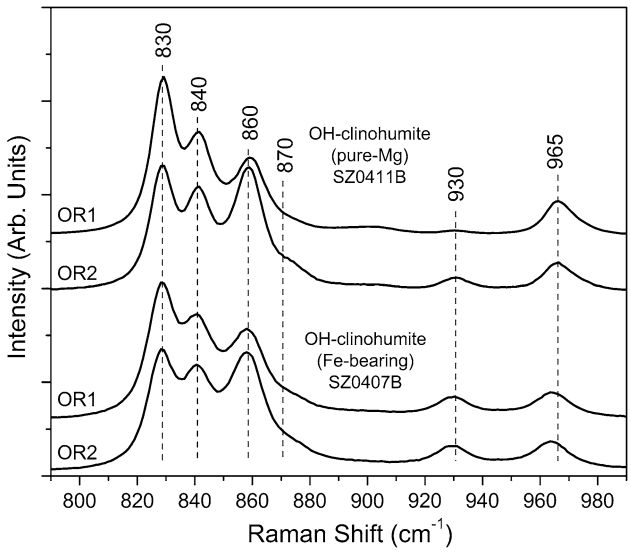

Fig. 4 Comparison of unpolarized Raman spectra between Mg-pure and Fe-bearing OH-clinohumite in the 800–1,000 cm^{-1} region for two different orientations of the sample

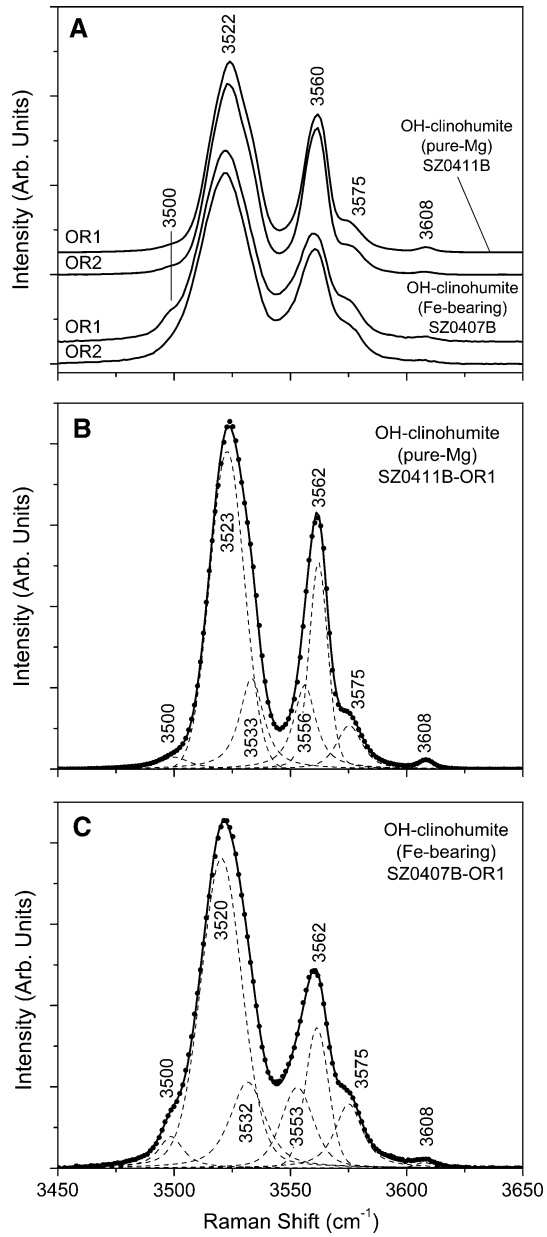

Fig. 5 a Comparison of unpolarized Raman spectra in the OH-stretching region between Mg-pure and Fe-bearing OH-clinohumite for two sample different orientations. *Panels B* and *C* illustrate deconvolution of the spectra into seven distinct OH-stretching modes

M3 site with almost equal Ti distribution in each octahedral site for F-free titano-clinohumite. On the other hand, Fujino and Takéuchi (1978) and Friedrich et al. (2001) indicate nearly equal distribution of Fe among the octahedral sites, but most of the Ti concentrated in the M3 site for their titano-clinohumite samples (Fe % $\approx$ 12 % and Ti % $\approx$ 5 %). Since Ti appears to order into M3, it is likely that the slight excess of Fe in M3 observed in SZ0407B may be due to a small amount of ferric iron as oxygen fugacity was not tightly controlled during the synthesis experiment. The refined Si1 and Si2 occupancies for SZ0407B are very close to those from SZ0411B (Mg-pure sample), and the Si occupancies in both samples are slightly less than one.

The bond lengths and volumes of cation polyhedra for the current samples were calculated using the software package XTALDRAW (Downs et al. 1993) and are listed in Table 5. The most significant differences in bond lengths between these two samples are as follows: M1C-O14, M1n-O13, M25-O24, M26-O14, and M3-O21 bond lengths from SZ0407B are 0.06, 0.07, 0.06, 0.06, and 0.010 Å longer than those from SZ0411B, respectively, consistent with higher ferrous iron contents. The two M3-OFOH bond lengths of SZ0407B are 0.011 and 0.008 Å shorter than those of SZ0411B, respectively, consistent with a small amount of ferric iron ordering into M3. Berry and James (2001) gave OF–D1 = 1.07(2) Å and OF–D2 = 1.08(2) Å for Mg-pure deuterated hydroxyl-clinohumite by powder neutron diffraction, while the current single-crystal X-ray diffraction studies show OF–H1 bond lengths of 0.99(6) Å for SZ0407B/0.84(6) Å for SZ0411B; and OF–H2 bond lengths of 1.35(Å) for SZ0407B/1.62(6) Å for SZ0411B, assuming full occupancies in H1/H2 sites. The H atomic positions refined from neutron diffraction better reflect the O–H interatomic distances compared with our results from X-ray diffraction.

To compare the effects of Fe, Ti, and F components on the crystal structure of clinohumite, the selected M–O bond

Table 5 Bond lengths (Å) and volumes (Å^3) of cation polyhedra

	SZ0407B	SZ0411B		SZ0407B	SZ0411B
M1C			*M3*		
O11 × 2	2.093(1)	2.096(2)	O21	2.142(1)	2.132(2)
O12 × 2	2.075(1)	2.073(2)	O22	2.241(1)	2.243(2)
O14 × 2	2.135(1)	2.129(2)	O24	2.020(1)	2.017(2)
Avg. bond	2.101(1)	2.099(2)	O24	2.116(1)	2.114(2)
Poly. *V* (Å^3)	11.90(1)	11.86(2)	OFOH	2.050(2)	2.061(3)
			OFOH	2.072(2)	2.080(3)
			Avg. bond	2.107(1)	2.108(2)
			Poly. *V* (Å^3)	12.10(1)	12.11(2)
M1N			*Si1*		
O11	2.113(1)	2.115(2)	O11	1.616(1)	1.614(2)
O12	2.083(1)	2.083(2)	O12	1.659(1)	1.654(2)
O13	2.126(1)	2.119(2)	O13	1.642(1)	1.640(2)
O21	2.099(1)	2.097(2)	O14	1.638(1)	1.637(2)
O22	2.070(1)	2.067(2)	Avg. bond	1.639((1)	1.636(2)
O23	2.139(1)	2.138(2)	Poly. *V* (Å^3)	2.22(1)	2.21(2)
Avg. bond	2.105(1)	2.103(2)			
Poly. *V* (Å^3)	11.95(1)	11.92(2)			
M25			*Si2*		
O13	2.034(1)	2.036(2)	O21	1.614(1)	1.613(2)
O21	2.192(1)	2.193(2)	O22	1.646(1)	1.644(2)
O22	2.067(1)	2.067(2)	O23	1.644(1)	1.640(2)
O23	2.185(1)	2.182(2)	O24	1.642(1)	1.642(2)
O24	2.211(1)	2.205(2)	Avg. bond	1.636(1)	1.635(2)
OFOH	2.066(2)	2.067(3)	Poly. *V* (Å^3)	2.22(1)	2.21(2)
Avg. bond	2.126(1)	2.125(2)			
Poly. *V* (Å^3)	12.43(1)	12.42(2)			
M26			*H1*		
O11	2.189(1)	2.184(2)	OFOH	0.99(6)	0.84(6)
O12	2.060(1)	2.060(2)	*H2*		
O13	2.198(1)	2.197(2)	OFOH	1.37(6)	1.62(6)
O14	2.243(1)	2.237(2)			
O14	2.058(1)	2.060(2)			
O23	2.074(1)	2.075(2)			
Avg. bond	2.137(1)	2.136(2)			
Poly. *V* (Å^3)	12.53(1)	12.50(2)			

lengths for samples of this and previous studies are summarized in Table 6. Ti has the most significant contribution to increasing the α angle (e, f, and g), while F decreases the unit-cell volumes most significantly (d and h). The most significant effect of these elements on M–O bond lengths is the decreasing in M3–OF lengths. The M3–OF bond lengths decrease in the order of a, c > b > g > h, d > e, f (Mg % = 100 % and Ti % = 0 for a and c; Fe % ~ 12 % and Ti % ~ 5 % for e and f), consistent with the radius of Mg^{2+} being larger than those of Fe^{3+} and Ti^{4+}. Consequently, ⟨M3–O⟩ bond lengths for samples d, e, f, g, and h are ~0.02 Å smaller than those of samples a and c, due to the shortened M3–OF lengths. ⟨M2-5–O⟩ lengths of samples e and f are ~0.01 Å larger than those of the other samples,

Table 6 Selected bond lengths (Å) for clinohumite samples of this study and from the literature

	Fe %*	Ti %*	F %$^+$	α (°)	*V* (Å^3)	OF$^\#$-M25	OF-M3(1)	OF-M3(2)	⟨M1C-O⟩	⟨M1N-O⟩	⟨M25-O⟩	⟨M26-O⟩	⟨M3-O⟩
a	0	0	0	100.638(9)	658.15(9)	2.067(3)	2.061(3)	2.080(3)	2.099(2)	2.103(2)	2.125(2)	2.136(2)	2.108(2)
b	4.1	0.01	0	100.645(9)	659.04(9)	2.066(2)	2.050(2)	2.072(2)	2.101(1)	2.105(1)	2.126(1)	2.137(1)	2.107(1)
c	0	0	0	100.639(1)	657.62(2)	2.046(11)	2.073(10)	2.092(9)	2.091(2)	2.102(5)	2.119(7)	2.141(5)	2.106(9)
d	5.6	0.2	5.8	100.786(2)	652.69(5)	2.064(7)	2.015(7)	2.040(7)	2.107(7)		2.109(7) 2.119(6)	2.136(7)	2.081(6)
e	11.6	5.2	0	101.00(2)	660.8(2)	2.056(5)	1.981(4)	2.000(5)	2.114(4)	2.108(5)	2.134(5)	2.140(5)	2.087(4)
f	12.1	5.1	0	101.00(2)	660.0(2)	2.053(2)	1.978(2)	1.988(2)	2.104(2)	2.108(2)	2.135(2)	2.138(2)	2.087(2)
g	0.06	2.4	3.7	100.909(8)	650.5(1)	2.057(2)	2.030(2)	2.050(2)	2.097(1)	2.101(2)	2.122(2)	2.131(1)	2.081(2)
h	0.6	0.6	9	100.84(3)	650.6(3)	2.058(2)	2.022(2)	2.040(2)	2.096(2)	2.101(2)	2.118(2)	2.130(2)	2.084(2)

a and b: SZ0411B and SZ0407B of the current study; c: Berry and James 2001; d and e: Robinson et al. 1973; f: Fujino and Takéuchi 1978; g: Friedrich et al. 2001; h: Ottolini et al. 2000

* Cation mole percentage in the total metallic cations

$^+$ Anion mole percentage in the total anions ($F^- + O^{2-}$)

$^\#$ OF is short for OFOH

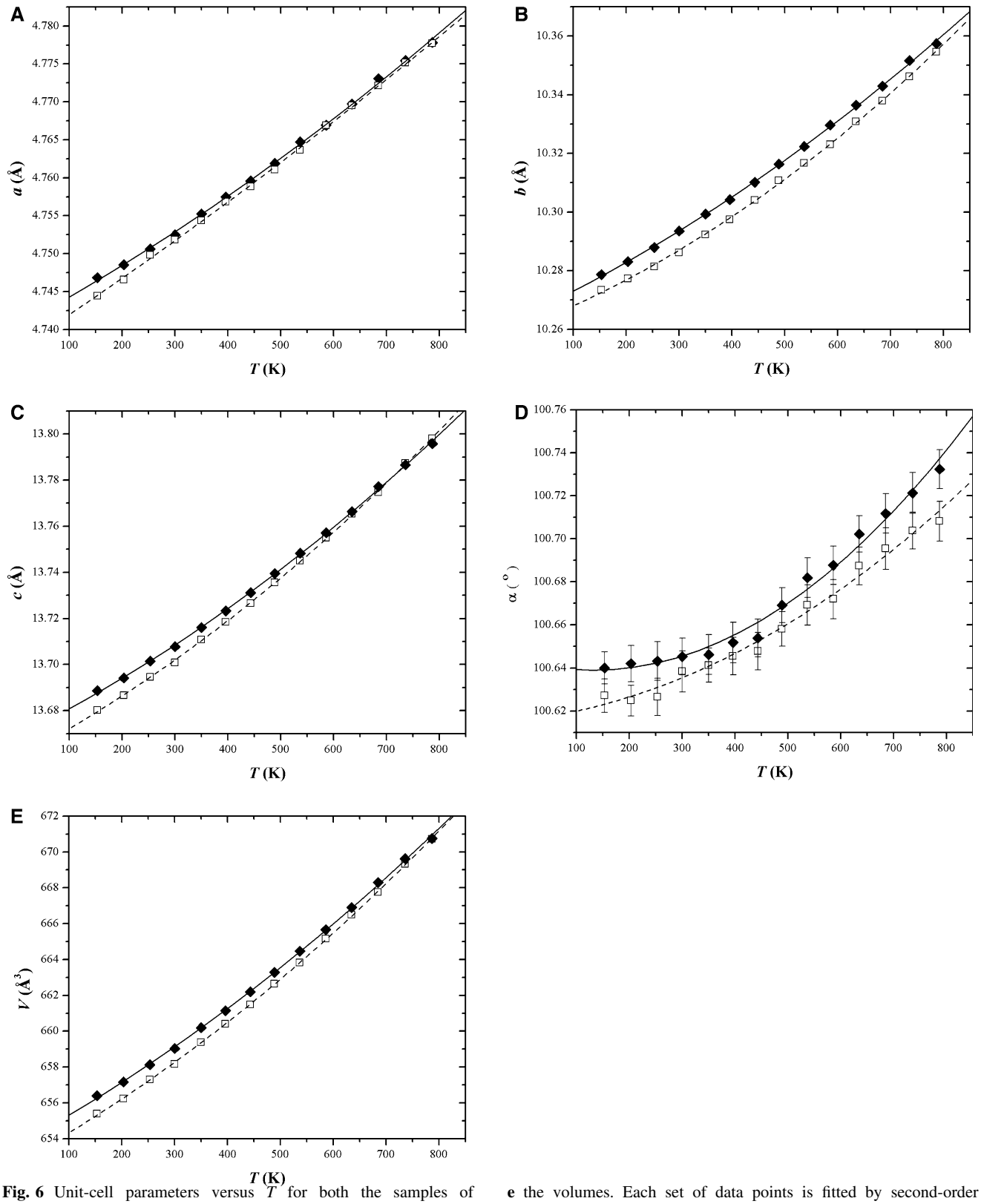

Fig. 6 Unit-cell parameters versus *T* for both the samples of SZ0407B (*solid diamond*) and SZ0411B (*open square*). **a–c** the axes; **d** α angles with *vertical error bars* for the uncertainties of the angles; **e** the volumes. Each set of data points is fitted by second-order polynomial curve (*solid* SZ0407B; *dash* SZ0411B)

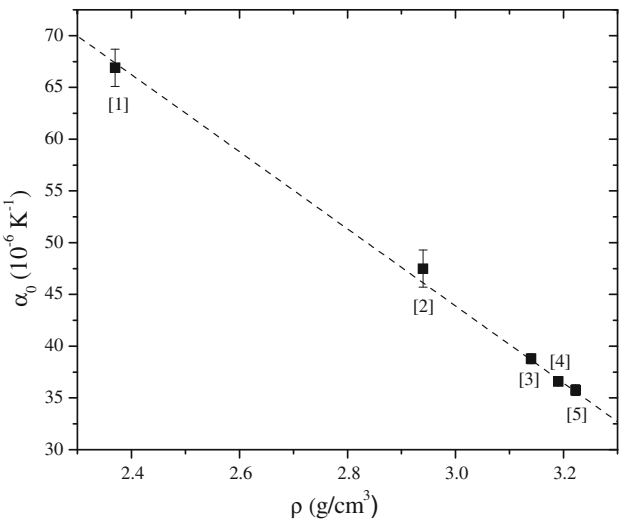

Fig. 7 Plot of average thermal expansion coefficient versus density for DHMS phases along the forsterite–brucite. *[1]* brucite, Fukui et al. (2003); *[2]* phase A, Pawley et al. (1995); *[3]* clinohumite, the current sample of SZ0411B; *[4]* clinohumite, the current sample of SZ0407B; *[5]* anhydrous forsterite, Ye et al. (2009). The temperature ranges are as follows: 299–593 K for Point *[1]*; 293–873 K for Point *[2]*; 300–787 K for Points *[3–5]*

consistent with higher contents of larger cations (Fe^{2+}) and no OF atoms coordinating with the M2-5 site. There are no significant differences for other ⟨M–O⟩ lengths among the samples.

Thermal expansion

The unit-cell parameters *a*, *b*, *c*, α, and *V* versus temperature are plotted in Fig. 6a–e, respectively, with second-order polynomial fitting for each data set. The calculated bulk, axial, and α angle thermal expansion coefficients are summarized in Table 7. Both samples show anisotropy of thermal expansion in the order of $\alpha_c > \alpha_b > \alpha_a$, while Ross and Crichton (2001) concluded the anisotropy of compressibility as $\beta_b > \beta_c > \beta_a$ for Mg-pure synthetic clinohumite. The α angles increase as temperature increases, especially above 450 K.

Prior studies of thermal expansivity of other DHMS phases along the brucite–forsterite join were reported for brucite (Fukui et al. 2003), Phase A (Pawley et al. 1995) and forsterite (Ye et al. 2009; and Smyth and Hazen 1973). The average thermal expansion coefficients (α_0) for these phases are summarized in Fig. 7, as a function of density. The linear regression gives a systematic relation with density:

$$\alpha_0(V)(10^{-6}\mathrm{K}^{-1}) = 156(7) - 37(2) \times \rho(\mathrm{g/cm}^3) \quad (1)$$

The negative slope of this regression is consistent with the positive slope of linear regression for isothermal bulk modulus (K_T) versus density (Ross and Crichton 2001 and Holl et al. 2006). The *Points [1, 2, 3 and 5]* are Mg-pure phases, and *Point [4]* has a Fe % of ~4 %, indicating that the $\alpha_0(V)$ versus ρ relationship appears to hold for at least some Fe-bearing phases such as clinohumite.

After heating to 787 K, each sample was cooled to room temperature to refine the unit-cell parameters again: $a = 4.7514(4)$ Å, $b = 10.293(1)$ Å, $c = 13.7045(9)$ Å, $\alpha = 100.648$ (9)°, $V = 658.71(9)$ Å^3 for SZ0407B; $a = 4.7513(6)$ Å, $b = 10.287(1)$ Å, $c = 13.7000(9)$ Å, $\alpha = 100.632(9)°$, $V = 658.15(9)$ Å^3 for SZ0411B, which are consistent with the initial unit-cell parameters before heating. In conclusion, both the single crystals of Mg-pure and Fe-bearing clinohumite persist to 787 K at ambient pressure, without significant phase transition or dehydration. In addition, Pawley et al. (1995) reported that the structure of Phase A persists to 873 K, and Ye et al. (2009)

Table 7 Bulk, axial, and α angle thermal expansion coefficients

	$\alpha = a_1{*}T + a_0$			$\alpha = \alpha_0$	
	a_1 (10^{-9} K^{-2})	a_0 (10^{-6} K^{-1})	R^2	α_0 (10^{-6} K^{-1})	R^2
SZ0407B					
V	21.4(19)	24.8(10)	0.9997	34.9(5)	0.9967
a	5.5(10)	7.9(4)	0.9992	10.5(1)	0.9970
b	8.5(8)	8.3(4)	0.9996	12.3(2)	0.9959
c	9.0(7)	8.3(4)	0.9997	12.5(2)	0.9957
α	4.6(6)	−0.6(3)	0.9845	1.53(13)	0.9157
SZ0411B					
V	25.4(13)	24.9(6)	0.9999	36.8(6)	0.9962
a	3.0(9)	9.7(4)	0.9994	11.1(1)	0.9988
b	12.4(9)	6.7(4)	0.9995	12.6(3)	0.9920
c	10.2(3)	8.9(3)	0.9998	13.7(3)	0.9955
α	2.4(4)	0.3(3)	0.9848	1.41(8)	0.9632

reported the persistence of hydrous forsterite (0.89 wt% H_2O) up to 919 K, also at ambient pressure.

The volume thermal expansion, $\alpha_0(V)$, for sample SZ0407B is about 2×10^{-6} K^{-1} smaller than that for SZ0411B, indicating that a 1 mol% increase in Fe content decreases the thermal expansivity by about 1.3 %, compared with Mg-pure clinohumite. Smyth and Hazen (1973) and Smyth (1975) demonstrated that Fe decreases the thermal expansivity of olivine. In addition, extensive high-pressure studies supported that Fe decreases the compressibilities or increases the isothermal bulk moduli of the silicates in the upper mantle and transition zone, such as Phase A (Crichton and Ross 2002; Holl et al. 2006), olivine (Zhang 1998), wadsleyite (Hazen et al. 1990), ringwoodite (Hazen 1993), and garnet (Hazen et al. 1994).

In summary, we have studied the high-temperature crystal chemistry of two hydroxyl-clinohumite: one pure-Mg sample and one with Fe/(Fe + Mg) of about 4 mol%. Synthesis conditions for both compositions were 12 GPa and 1,250 °C, corresponding to conditions near 360 km depth in a hydrous subducting slab. Refinement of the crystal structures at ambient conditions shows a small volume increase in octahedral cation sites M1c, M1n, M2-5, and M2-6 consistent with ferrous iron substitution into these sites and a slight volume decrease in M3 consistent with a small amount of ferric iron ordering into this site. We have measured thermal expansion of these two samples from 157 to 787 K and observe a small decrease in expansivity with iron substitution. Comparing thermal expansivity with other DHMS phases on the forsterite–brucite join, we derive a systematic relationship of thermal expansivity with density consistent with previous observation of a systematic variation of compressibility with density.

Acknowledgments This work was supported by US National Science Foundation grant EAR 11-13369 to JRS. SDJ acknowledges support from the NSF EAR-0748707 (CAREER), the Carnegie/DOE Alliance Center (CDAC), and by the David and Lucile Packard Foundation. Syntheses were performed at Bayerisches Geoinstitut, University of Bayreuth, Germany, and supported in part by the Alexander von Humboldt Foundation.

Appendix

See Table 8.

Table 8 Unit-cell parameters as functions of temperature for both samples SZ0407B and SZ0411B

T(K)	*a* (Å)	*b* (Å)	*c* (Å)	α (°)	*V* (Å^3)
SZ0407B					
153(2)	4.7468(4)	10.279(1)	13.6887(8)	100.641(8)	656.40(8)
203(2)	4.7485(4)	10.283(1)	13.6942(9)	100.643(8)	657.17(8)
253(2)	4.7506(4)	10.288(1)	13.7015(9)	100.643(9)	658.13(8)
300(2)	4.7525(4)	10.294(1)	13.7077(9)	100.645(9)	659.04(9)
350(2)	4.7552(4)	10.299(1)	13.7161(9)	100.646(9)	660.19(9)
396(3)	4.7575(4)	10.304(1)	13.7232(9)	100.652(9)	661.15(9)
443(3)	4.7596(4)	10.310(1)	13.7312(9)	100.654(9)	662.20(8)
489(3)	4.7619(4)	10.316(1)	13.7395(9)	100.669(8)	663.28(8)
537(4)	4.7647(4)	10.322(1)	13.7482(9)	100.682(9)	664.46(9)
586(4)	4.7669(4)	10.330(1)	13.7571(9)	100.688(9)	665.66(8)
635(4)	4.7697(4)	10.336(1)	13.7664(9)	100.702(8)	666.90(8)
685(4)	4.7731(4)	10.343(1)	13.7772(9)	100.712(9)	668.29(9)
736(5)	4.7754(4)	10.352(1)	13.7866(9)	100.721(9)	669.62(9)
787(5)	4.7778(4)	10.357(1)	13.7958(9)	100.732(9)	670.75(9)
SZ0411B					
153(2)	4.7444(6)	10.273(1)	13.6802(8)	100.627(8)	655.39(9)
203(2)	4.7466(5)	10.277(1)	13.6866(9)	100.625(7)	656.23(8)
253(2)	4.7498(6)	10.281(1)	13.6946(9)	100.627(9)	657.30(9)
300(2)	4.7518(6)	10.286(1)	13.7008(9)	100.638(9)	658.15(9)
350(2)	4.7544(5)	10.292(1)	13.7108(9)	100.641(8)	659.38(9)
396(3)	4.7568(6)	10.297(1)	13.7185(9)	100.646(9)	660.41(9)
443(3)	4.7588(6)	10.304(1)	13.7265(9)	100.648(9)	661.49(9)
489(3)	4.7610(5)	10.311(1)	13.7355(9)	100.658(8)	662.64(9)
537(4)	4.7636(6)	10.317(1)	13.7450(9)	100.669(9)	663.82(9)
586(4)	4.7669(6)	10.323(1)	13.7549(9)	100.672(9)	665.16(9)
635(4)	4.7695(6)	10.331(1)	13.7653(9)	100.687(9)	666.49(9)
685(4)	4.7721(7)	10.338(1)	13.7747(9)	100.695(9)	667.76(9)
736(5)	4.7752(6)	10.346(1)	13.7874(9)	100.704(8)	669.31(9)
787(5)	4.7777(6)	10.355(1)	13.7980(9)	100.708(9)	670.72(9)

References

Berry AJ, James M (2001) Refinement of hydrogen positions in synthetic hydroxyl-clinohumite by powder neutron diffraction. Am Mineral 86:181–184

Crichton WA, Ross NL (2002) Equation of state of dense hydrous magnesium silicate phase A, $Mg_7Si_2O_8(OH)_6$. Am Mineral 87:333–338

Cromer DT, Mann J (1968) X-ray scattering factors computed from numerical Hartree-Fock wave functions. Acta Crystallogr A24:321–325

Downs RT, Bartelmehs KL, Gibbs GV, Boisen MB (1993) Interactive software for calculating and displaying X-ray or neutron powder diffractometer patterns of crystalline materials. Am Mineral 78:1104–1107

Farrugia LJ (1999) WinGX software package. J Appl Crystallogr 32:837–838

Faust J, Knittle E (1994) Static compression of chondrodite: implications for water in the upper mantle. Geophys Res Lett 21:1935–1938

Ferraris G, Prencipe M, Sokolova E, Gekimyants VM, Spiridonov E (2000) Hydroxyl-clinohumite a new member of the humite group: twinning, crystal structure and crystal chemistry of the clinohumite subgroup. Z für Krist 215:169–174

Friedrich A, Lager GA, Kunz M, Chakoumakos BC, Smyth JR, Schultz AJ (2001) Temperature-dependent single-crystal neutron diffraction study of natural chondrodite and clinohumite. Am Mineral 86:981–989

Fujino K, Takéuchi Y (1978) Crystal chemistry of titanian chondrodite and titanian clinohumite of high-pressure origin. Am Mineral 63:535–543

Fukui T, Ohtaka O, Suziki T, Funakoshi K (2003) Thermal expansion of $Mg(OH)_2$ brucite under high pressure and pressure dependence of entropy. Phys Chem Miner 30:511–516

Hazen RM (1993) Comparative compressibilities of silicate spinels: anomalous behavior of $(Mg, Fe)_2SiO_4$. Science 259:206–209

Hazen RM, Zhang J, Ko J (1990) Effects of Fe/Mg on the compressibility of synthetic wadsleyite: β-$(Mg_{1-x}Fe_x)_2SiO_4$ ($x \leq 0.25$). Phys Chem Miner 17:416–419

Hazen RM, Downs RT, Conrad PG, Finger LW, Gasparik T (1994) Comparative compressibilities of majorite-type garnets. Phys Chem Miner 21:344–349

Holl CM, Smyth JR, Manghnani MH, Amulele GM, Sekar M, Frost DJ, Prakapenka VB, Shen G (2006) Crystal structure and compression of an iron-bearing Phase A to 33 GPa. Phys Chem Miner 33:192–199

Kanzaki M (1991) Stability of hydrous magnesium silicates in the mantle transition zone. Phys Earth Planet Inter 66:307–312

Lin CC, Liu LG, Mernagh TP, Irifune T (2000) Raman spectroscopic study of hydroxyl-clinohumite at various pressures and temperatures. Phys Chem Miner 27:320–331

Liu Z, Lager GA, Hemley RJ, Ross NL (2003) Synchrotron infrared spectroscopy of OH-chondrodite and OH-clinohumite at high pressure. Am Mineral 88:1412–1415

McGetchin TR, Silver LT, Chodos AA (1970) Titanoclinohumite: a possible mineralogical site for water in the upper mantle. J Geophys Res 75:255–259

Ottolini L, Cámara F, Bigi S (2000) An investigation of matrix effects in the analysis of fluorine in humite-group minerals by EMPA, SIMS, and SREF. Am Mineral 85:89–102

Pawley AR, Redfern SAT, Wood BJ (1995) Thermal expansivities and compressibilities of hydrous phases in the system MgO-SiO_2-H_2O: talc, phase A and 10-Å phase. Contrib Mineral Petrol 122:301–307

Robinson K, Gibbs GV, Ribbe PH (1973) The crystal structure of the humite minerals IV. Clinohumite and Titanoclinohumite. Am Mineral 58:43–49

Ross NL, Crichton WA (2001) Compression of synthetic hydroxylclinohumite $[Mg_9Si_4O_{16}(OH)_2]$ and hydroxylchondrodite $[Mg_5Si_2O_8(OH)_2]$. Am Mineral 86:990–996

Sanchez-valle C, Sinogeikin SV, Smyth JR, Bass JD (2006) Single-crystal elastic properties of dense hydrous magnesium silicate phase A. Am Mineral 91:961–964

Sheldrick GM (1997) SHELXL97, Release 97-2. Program for the refinement of crystal structures. University of Göttingen, Germany

Smyth JR (1975) The high temperature crystal chemistry of fayalite. Am Mineral 60:1092–1097

Smyth JR, Hazen RM (1973) The crystal structure of forsterite and hortonolite at several temperatures up to 900°C. Am Mineral 58:588–593

Smyth JR, Frost DJ, Nestola F, Holl CM, Bromiley G (2006) Olivine hydration in the deep upper mantle: effects of temperature and silica activity. Geophys Res Lett 33:L15301

Tokonami M (1965) Atomic scattering factor for O^{2-}. Acta Crystallogr 19:486

Wunder B (1998) Equilibrium experiments in the system MgO–SiO_2–H_2O (MSH): stability fields of clinohumite-OH $[Mg_9Si_4O_{16}(OH)_6]$, chondrodite-OH $[Mg_5Si_2O_8(OH)_2]$ and phase A $[Mg_7Si_2O_8(OH)_6]$. Contrib Mineral Petrol 132:111–120

Wunder B, Medenbach O, Daniels P, Schreyer W (1995) Frist synthesis of the hydroxyl end-member of humite, $Mg_7Si_3O_{12}(OH)_2$. Am Mineral 80:638–640

Ye Y, Schwering RA, Smyth JR (2009) Effects of hydration on thermal expansion of forsterite, wadsleyite, and ringwoodite at ambient pressure. Am Mineral 94:899–904

Zhang L (1998) single crystal hydrostatic compression of (Mg, Mn, Fe, Co)2SiO4 olivines. Phys Chem Miner 25:308–312